JOURNAL OF THERMOPHYSICS AND HEAT TRANSFER
Vol. 24, No. 4, October–December 2010

Computational Analysis of Arc-Jet Stagnation Tests Including Ablation and Shape Change

Tahir Gökçen,* Yih-Kanq Chen,† Kristina A. Skokova,‡ and Frank S. Milos§
NASA Ames Research Center, Moffett Field, California 94035

DOI: 10.2514/1.46199

Coupled fluid-material response analyses of arc-jet stagnation tests conducted in a NASA Ames Research Center arc-jet facility are considered. The fluid analysis includes computational Navier–Stokes simulations of the nonequilibrium flowfield in the facility nozzle and test box as well as the flowfield over the models. The material response analysis includes simulation of two-dimensional surface ablation and internal heat conduction, thermal decomposition, and pyrolysis gas flow. For ablating test articles including shape change, the material response and fluid analyses are coupled to take into account changes in surface heat flux and pressure distributions with shape. The ablating material used in these arc-jet tests was a phenolic impregnated carbon ablator. Computational predictions of surface recession, shape change, and material response are compared with the experimental measurements.

Nomenclature

C_H = heat transfer coefficient, $q_w/(h_o - h_w)$, kg/(m^2.s)
c_i = mass fraction of species i
d = model diameter, cm
h = enthalpy, MJ/kg
h_o = total enthalpy, MJ/kg
h_{ocl} = centerline total enthalpy, MJ/kg
$\bar{h}_o$ = mass-averaged total enthalpy, $\int \rho u h_o \, dA / \int \rho u \, dA$, MJ/kg
h_w = wall enthalpy, MJ/kg
I = arc current, Amp
M = Mach number
$\dot{m}$ = mass flow rate, g/s
p = pressure, Pa or kPa
p_o = total or stagnation pressure, kPa
p_{o2} = model stagnation pressure or pitot pressure, kPa
p_s = model surface pressure, kPa
q_w = model surface heat flux, W/cm^2
r = radial coordinate, m
r_c = model corner radius, cm
r_n = nose radius of a test article, cm
s = arc length coordinate, m
s_{rec} = recession normal to the surface, cm
$s_{\text{rec}x}$ = recession in the model axial direction or x-direction, cm
T = temperature or translational-rotational temperature, K
T_s = model surface temperature, K
$T_{s\,\max}$ = maximum surface temperature at the stagnation point, K
T_v = vibrational or vibrational-electronic temperature, K
t = time, s
V = arc voltage, Volt
ϵ = hemispherical emissivity
ρ = density, kg/m^3
ρ_v = density of virgin material, kg/m^3

Presented as Paper 2009-3596 at the 41st AIAA Thermophysics Conference, San Antonio, TX, 22–25 June 2009; received 30 June 2009; revision received 21 April 2010; accepted for publication 22 April 2010.

*ELORET Corporation, MS 230-2, Senior Research Scientist. Senior Member AIAA.
†Aerospace Engineer, Thermal Protection Materials and Systems Branch. Member AIAA.
‡ELORET Corporation, Senior Research Scientist, Principal Investigator for CEV Arc-Jet Tests.
§Aerospace Engineer, Thermal Protection Materials and Systems Branch. Senior Member AIAA.

I. Introduction

ARC-JET facilities provide the primary means to test the performance of various types of thermal protection system (TPS) materials and configurations used on the outer surfaces of spacecraft in an aerothermodynamic heating environment. Thermal, chemical and morphological stability of the TPS surface in locations such as the nose cap and wing leading edge is particularly important. In a high enthalpy arc-jet facility, a test gas, usually air or a mixture of nitrogen, oxygen and argon, is passed through an electric arc discharge where energy is added to the flow. The test gas is then expanded through a converging-diverging nozzle into an evacuated test chamber to produce high-enthalpy hypersonic flow. NASA Ames Research Center has a number of arc-jet facilities within its Arc-Jet Complex that have long been used in development and testing of TPS for entry vehicles such as the Space Shuttle Orbiter and planetary probes [1–5].

Development of efficient real gas computational fluid dynamics (CFD) codes and advances in computer technology in recent years have enabled CFD analysis to become an integral part of arc-jet testing. Arc-jet test configurations have also evolved from simple coupon or panel geometries of the past to increasingly complex geometries designed for aerothermodynamic simulation, and computational simulations are used from the planning stages of the arc-jet experiments through posttest analysis. Recent examples of such CFD analysis for complex arc-jet test configurations were reported in [6–9]. For these arc-jet test articles, material thermal response simulations were decoupled from the CFD computations. However, if the TPS material is ablating and changing shape with time, the thermal response/ablation model and CFD analysis need to take into account the changes in the surface heat flux and pressure distributions on the test article due to the shape change. For certain arc-jet tests, the shape change and its effect on the surface heat flux and pressure distributions are relatively small, and decoupled simulations may be adequate. Generally, though, the heat flux and its distribution are sensitive to the shape of the test article. Therefore, when there is any significant shape change during a test, fluid dynamics and solid thermochemical simulations need to be coupled [10].

The primary objective of the present paper is to report coupled CFD/material response analyses of ablation tests conducted in a

NASA Ames arc-jet facility. The ablating material used in these tests was Phenolic Impregnated Carbon Ablator (PICA), which is a low density TPS material developed at NASA Ames Research Center in the 1990s [11,12]. PICA was used to construct the heatshield for the Stardust sample-return capsule and the Mars Science Laboratory entry vehicle. It was also one of the two final candidate heatshield materials for the Orion Crew Exploration Vehicle. Therefore, the Orion TPS Advanced Development Project conducted a large number of arc-jet tests to evaluate its performance over a wide range of aerothermal heating conditions, and a database was generated for development and validation of the PICA thermal response/ablation model [13,14].

For the present paper, three sets of PICA tests, on stagnation models with ablation and varying degrees of shape change, are considered. Whether CFD and material response model analyses are coupled or decoupled, they are useful for interpretation of the test data, and along with the test data, to define arc-jet test environments. Ultimately, these analyses provide a method for the traceability of the TPS performance from a ground test facility to flight. Because of the ablation and shape change that occur in these tests, coupled fluid-material response analyses are necessary. The present CFD analysis comprises simulations of the nonequilibrium flowfield in the arc-jet facility (nozzle, test box, over the model). The material response analysis includes simulation of two-dimensional surface ablation and internal heat conduction, thermal decomposition, and pyrolysis gas flow. For these simulations, the CFD and material response codes are loosely coupled. Briefly, this means that the CFD simulations are started with the unablated shape, and its surface heat flux and pressure distributions are computed; after that, the material response model is run until a predetermined recession level is reached. Then, a new CFD grid is generated using the ablated surface, and a new CFD solution using this grid is computed. Subsequently, the heat flux and pressure distributions used in the material response model are updated, and the procedure is repeated until the prescribed test time is reached. The total number of iterations depends on the total surface recession; for some cases, several hundred iterations are performed via a scripted process. The paper presents comparisons of predicted recession and in-depth temperatures with the experimental measurements for three cases.

II. Arc-Jet Facility and Test Data

NASA Ames Research Center has several arc-jet facilities within its Arc-Jet Complex. Of these, the 60-MW Interaction Heating Facility (IHF) has the highest power rating. The IHF was originally constructed to test relatively large-scale models at the peak heating conditions of the Space Shuttle Orbiter atmospheric entry. Figure 1 shows a schematic diagram of the IHF and its nozzle configurations. The IHF consists of a constricted arc heater, a 60-MW DC power supply, interchangeable conical and semi-elliptical nozzles, a test box or chamber, and supplementary systems, including a steam ejector vacuum system, a cooling-water system and a data acquisition system. The IHF is designed to operate with a set of conical nozzles or a semi-elliptical nozzle at total pressures of 1–9 atm and total enthalpies of 7–47 MJ/kg (air) [1–5]. The 60-MW constricted arc heater produces high-temperature test gas for both nozzles. The conical nozzle configurations of the IHF are suitable for tests of stagnation coupon and blunted wedge test articles, while the semi-elliptical nozzle configuration is designed mainly for testing flat panels in boundary-layer heating environments. Further information on the Ames IHF and other arc-jet facilities can be found in Refs. [1–5].

An axisymmetric blunted model in a conical nozzle flow is one of the most frequently employed arc-jet test configurations. A photograph of a stagnation arc-jet test is shown in Fig. 2. To characterize the aerothermodynamic heating environment over the test article, a calorimeter with the same geometry as the test article is usually used to measure the surface heat flux and pressure, and the test articles are instrumented with a number of thermocouples. The standard facility/calibration data include measurements of total pressure (arc heater pressure), mass flow rate, total bulk enthalpy, test box pressure, and stagnation-point calorimeter heat flux and pitot pressure. CFD simulations along with the stagnation-calorimeter measurements provide an estimate of the centerline total enthalpy [8,9].

The tests reported here used the IHF 13-inch-diameter conical nozzle, which has a throat diameter of 6.033 cm (2.375 in). The diverging section of the nozzle has a half-angle of 10° with an exit diameter of 33.02 cm (13 inches). Three sets of ablation tests are considered. First, a 10.16-cm diameter iso-q (constant heat flux) stagnation model tested 25.4 cm downstream of the nozzle exit is

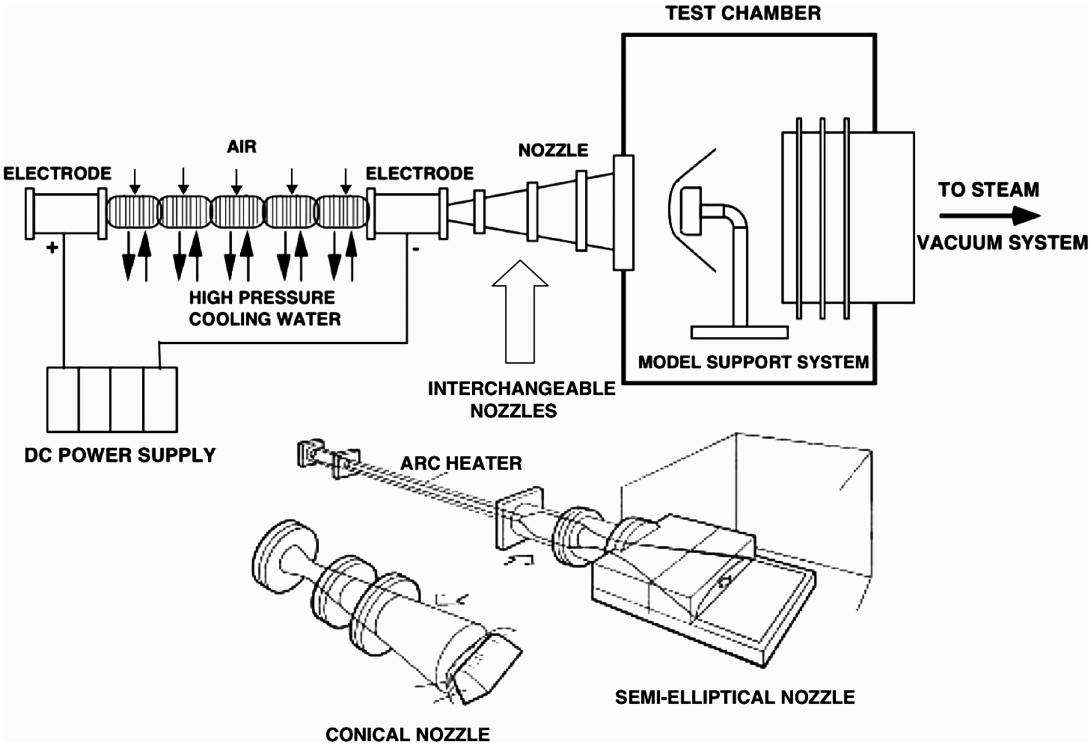

Fig. 1 Sketches of the NASA Ames Research Center 60-MW IHF and its interchangeable nozzle configurations.

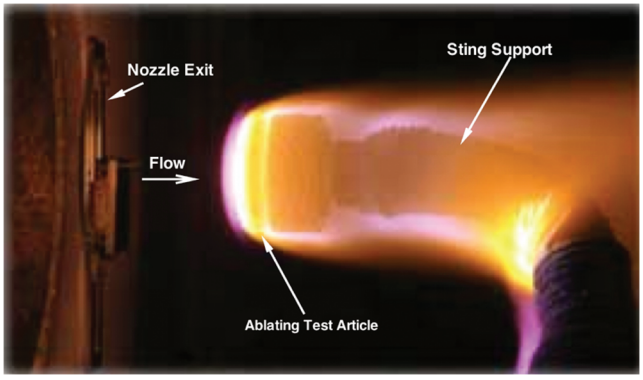

Fig. 2 A photograph of a stagnation model with ablating test article in the IHF.

considered (IHF 184 tests). This iso-q model consists of a spherical segment nosecap, with nose radius equal to the model diameter, and a cylindrical body aligned with the flow. The shoulder region of the nosecap is rounded to the cylindrical sides ($r_c/r_n = 1/16$). Second, a 12.7-cm diameter flat-faced model ($r_c = 0.635$ cm) tested 25.4 cm downstream of the nozzle exit is considered (IHF 198 tests). Finally, a 10.16-cm diameter flat-faced model ($r_c = 0.953$ cm) tested 10.16 cm downstream of the nozzle exit is considered (IHF 121 tests). The first two models were tested by the Orion TPS project, and they include moderate levels of surface recession and shape change; the last model was tested by Covington et al. [12] and it had a larger amount of recession and shape change.

III. Computational Approach

Building blocks of the present computational analysis are: 1) steady-state CFD simulation of nonequilibrium expanding flow in the IHF nozzle and supersonic jet, and flowfield around arc-jet test articles, and 2) the material response simulation of the test article.

The Data Parallel Line Relaxation (DPLR) code [15][¶] is used for computations of the nonequilibrium flow in the nozzle and flowfield around test articles. DPLR has been used extensively at NASA Ames Research Center for hypersonic flight and planetary entry simulations, and its results have been compared against a wide variety of flight and ground-based experiments. DPLR provides various options for thermophysical models and formulation. For CFD calculations presented in this paper, the 2-D axisymmetric Navier–Stokes equations, supplemented with the equations accounting for nonequilibrium kinetic processes, are used in the formulation. The present thermochemical model for arc-jet flow includes six species (N_2, O_2, NO, N, O, Ar), and the thermal state of the gas is described by two temperatures within the framework of Park's two-temperature model [16,17]. In the two-temperature model, excitations of internal degrees of freedom are divided into two classes, and it is assumed that excitations are equilibrated within each class. The translational and rotational modes of energy make up one class, and it is characterized by a translational-rotational temperature, T. The vibrational and electronic modes form the other class, and it is characterized by a vibrational-electronic temperature, T_v.

The flowfield in an arc-jet facility, from the arc heater to the test section, is a very complex, three-dimensional flow coupled to various nonequilibrium processes. To simulate the flowfield, several simplifying assumptions are made, and corresponding numerical boundary conditions are prescribed for CFD simulations. Briefly, the present nozzle simulations are started from the nozzle throat, and the flow properties at the throat are assumed to be uniform and those at thermochemical equilibrium. The total enthalpy of the arc-jet test flow (and its distribution) is usually inferred from facility and calibration measurements. The facility data include measurements of total pressure, mass flow rate, total bulk enthalpy, and test box pressure; the calibration data include stagnation-point calorimeter heat flux and pitot pressure. For the present CFD simulations, the total enthalpy levels and its distribution are set such that the computations reproduce the facility and calibration data as well as possible (in particular, the measured stagnation-point heat flux and pressure). Further details of the assumptions made and numerical boundary conditions imposed in simulations can be found in [6–9]. As a typical stagnation test simulation result, Fig. 3 shows computed flowfield of the IHF 13-inch-diameter conical nozzle flow with a calorimeter model placed 25.4 cm downstream of the nozzle exit. Because of the nonequilibrium expansion process in arc-jet nozzles, the chemical composition freezes near the throat where the flow is dissociated and and vibrationally excited. As shown in Fig. 3b, the computations also predict that the flow is chemically and vibrationally frozen before it reaches the nozzle exit. Note that oxygen remains fully dissociated within the entire flowfield except in the boundary layer near the walls, while nitrogen is partially dissociated.

The Two-Dimensional Implicit Thermal Response and Ablation Program (TITAN) [18] is used for computing the material response of the test articles. In TITAN, the two-dimensional energy conservation equation, a three-component decomposition model, and the surface energy balance are solved with a moving grid to predict the thermal response and surface recession of charring materials. The internal energy equation is a transient thermal conduction equation with additional terms due to convection of the pyrolysis gas. The three-component solid model for organic resin composites consists of a general mixture of a two-component resin and a reinforcing material. Each of these components decomposes independently by a reaction rate. Virgin (original) and char (residual) density and thermal properties of each component are specified as functions of temperature, pressure (and orientation for conductivity). Thermochemical conditions at the ablating surface are determined by the aerothermal flow environment and by chemical interactions between the boundary layer gas, the pyrolysis gas, the ablation products, and the chemical constituents of the surface material. TITAN employs a convective transfer-coefficient form of the surface energy balance to determine the surface conditions, and uses a blowing correction to account for the reduction in heat transfer coefficient (predicted by CFD) due to the injection of gases from pyrolysis and surface ablation. TITAN has also been used extensively at Ames for various simulations of hypersonic flight, planetary entry and arc-jet experiments [10,13,14,19,20]. For all PICA material response simulations in this paper, the PICAv3.3 material property model developed by Milos and Chen [13] is used. The PICAv3.3 model includes effects of orthotropic thermal conductivity (through-the-thickness and in-plane thermal conductivities), and further information on the model and its validation can be found in [13,14].

The DPLR and TITAN simulations are loosely coupled. In this approach, the simulation is started with the unablated shape and its heat flux and pressure distributions. Then, when a predetermined recession level predicted by TITAN is reached at any location on the model, a new CFD solution using a new grid for the ablated shape is computed. The heat flux and pressure distributions used in TITAN are updated, and the procedure is repeated until the prescribed test time is reached. CFD simulations are performed using fully catalytic cold wall boundary conditions. For each TITAN simulation, only distributions of the surface heat flux q_w or the heat transfer coefficient C_H, the surface pressure p_s, and total enthalpy h_o estimated by CFD simulations are used. The TITAN simulation provides predictions of the surface temperature and recession, and the intermediate surface coordinates to update the computational grid. The grids for all CFD simulations are generated through a *Gridgen* [21] script. The entire simulation (DPLR, TITAN and *Gridgen*) is performed by making use of a UNIX shell script. For the present simulations, the model surface and subsequent CFD simulations are updated whenever the maximum recession in the TITAN simulation reaches 0.05 mm. This means that for a 1 cm total recession at any location on the model, 200 *Gridgen*, DPLR and TITAN simulations are performed.

[¶]Private communication with M. J. Wright, "Data-Parallel Line Relaxation (DPLR) Code," Version 3.05, June 2006.

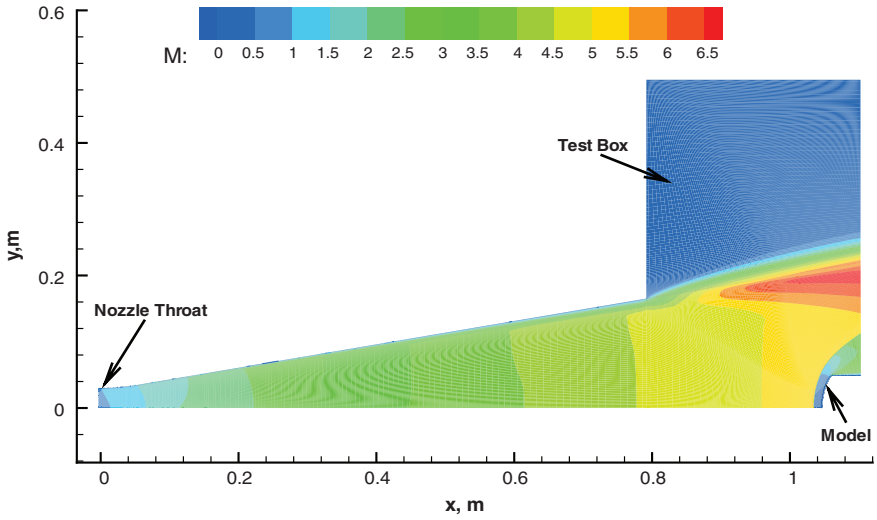

a) Mach number contours

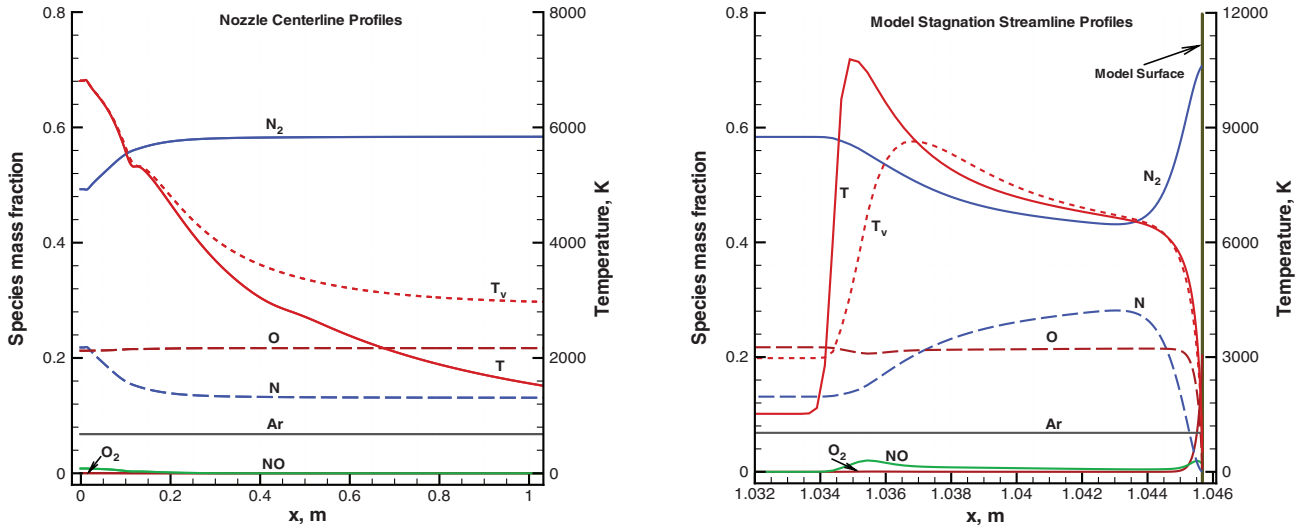

b) Flow properties along the nozzle centerline and model stagnation streamline

Fig. 3 Computed IHF 13-inch-diameter nozzle flow downstream of the throat and flowfield over a calorimeter model: $p_o = 466$ kPa, $h_o = 21.4$ MJ/kg, and 6.8% Ar in air.

IV. Presentation of Computed Results

Results of the computational analyses for the following three stagnation models are presented: 1) a 10.16-cm diameter iso-q model, 2) a 12.17-cm diameter flat-faced model, and 3) a 10.16-cm diameter flat-faced model. The test data for all three models include surface temperature (pyrometer) and surface recession measurements. For the two 10.16-cm models, they also include in-depth (thermocouple) temperature. The arc-jet data and the CFD estimates for three cases are summarized in Table 1. For each test case, computed results and comparisons with the test data are presented in the following sections.

A. Case 1: 10.16-cm Diameter Iso-Q Model

Numerous stagnation ablation tests have been conducted by the Orion TPS project over the last few years. Most of these tests were performed using the so-called iso-q shaped models. The iso-q model tests (IHF 184 tests) were run to evaluate performance of PICA at nominal heating conditions of 395 W/cm^2 and 17.2 kPa (stagnation-point cold wall heat flux and pressure). Based on the facility and stagnation-calorimeter measurements, the centerline total enthalpy of the arc-jet test flow is estimated to be 21.4 MJ/kg through CFD simulations.

Figure 4 shows the computed Mach number contours of the IHF 13-inch nozzle flow downstream of the nozzle exit. Also, in Fig. 4, the material map used for thermal response model simulations is shown. This detailed material map is implemented so as to reproduce the measured in-depth temperatures. The model holder is made of LI-2200 tile. The air gap between the PICA and the tile is needed to accommodate the thermocouples. The backface of the tile is assumed to be insulated.

In Fig. 5, the computed temperature contours and surface temperatures of the iso-q model are shown at two different test times, $t = 0.3$ and 34 s. At $t = 0.3$ s, the model is still relatively cold. The temperature discontinuity on the aft flank of the model is due to two different materials with different emissivities and thermal conductivities. Up to $t = 34$ s, the surface temperature of the model gradually increases, and as a result, the surface recession occurs. The heat penetration depth is clearly seen in the temperature contour plot. The time $t = 34$ s represents the end of the test; the ablated model is taken out of the arc-jet stream, and it starts to cool down.

Figure 6 shows comparisons of computed recession profiles and in-depth temperatures with the measurements. For IHF 184 tests, the stagnation-point recession was measured manually, and the recession profiles were obtained by use of laser scans of the pre and posttest models. For practical reasons, all recession measurements

Table 1 Summary of the arc-jet facility/test data and estimates for the IHF tests

Test	IHF 184	IHF 198	IHF 121
Model	Iso-q	Flat-faced	Flat-faced
d, cm	10.16	12.70	10.16
r_c, cm	0.635	0.635	0.953
Facility/test data			
p_o, kPa	466	824	906
I, Amp	2573	4504	6078
V, Volt	5736	6846	7249
$\dot{m}$, g/s	483	822	867
c_{Ar}, %	6.8	6.5	6.0
$\bar{h}_o$, MJ/kg	17.3	23.1	25.6
p_{o2}, kPa	17.2	32.7	45.6
q_{cw}, W/cm^2	395	440	580
t, s	34	40	69–86
s_{rec}, cm	0.452	0.543	1.22–1.46
$T_{s\,\max}$, K	2726	2849	2753–2833
In-depth thermocouples	yes	no	yes
Computational estimates			
h_{ocl}, MJ/kg	21.4	27.3	26.9
t, s	34	40	69–86
s_{rec}, cm	0.421	0.463	1.425–1.839
$T_{s\,\max}$, K	2761	2892	3166–3186

were linear recession measurements, i.e., the recession along the axial direction of the model, $s_{\mathrm{rec}x}$. The surface recession normal to the model surface, s_{rec}, differs from $s_{\mathrm{rec}x}$ away from the stagnation point of the model. In Fig. 6a, the measured and computed linear recession profiles at $t = 34$ s are compared. The measurements were obtained for the four quadrants of the model: center to top, bottom, left, and right (denoted as CB, CL, CT, and CR). There were two iso-q models tested at this nominal condition, and the measured stagnation-point recession at $t = 34$ s for these models were 0.4614 and 0.4427 cm. The computed stagnation-point recession at $t = 34$ s is 0.4205 cm, an underprediction of the measurements by approximately 5–9%. Note that both computed and measured linear recession profiles are relatively flat, although the computed normal recession actually gradually decreases away from the stagnation point, closely mimicking the surface heat flux distribution. In Fig. 6b, computed in-depth temperatures are compared with thermocouple measurements. The thermocouples (TC1, TC2, TC3, TC4, TC5) were placed along the centerline of the model at depths of 0.470, 0.889, 1.270, 1.676, and 3.048 cm, respectively, from the surface. Considering the recession is underpredicted, the agreement between the computed and measured in-depth temperatures is remarkably good. This is primarily because the amount of total recession is relatively small in comparison with the original PICA material depth; as a result, the computed in-depth temperatures are not significantly affected by the surface recession mismatch. The model surface temperatures were also measured using one-color (Mikron M190H: 0.78–1.06 μm) and two-color (Mikron M190 R2: 0.78–1.06 μm and 0.9–1.06 μm) pyrometers, and there were 2–3% differences between pyrometer measurements. One-color pyrometer measurements in the IHF were found to be more reliable, and the maximum surface temperatures measured by the one-color pyrometer were listed in Table 1. The reported temperatures include corrections for window losses and PICA emissivity ($\epsilon = 0.931$). The computed surface temperatures are in reasonably good agreement with the measurements.

Figure 7 shows the computed surface heat flux and pressure distributions for both nominal and recessed models. The predicted heat flux values on the front face of the models are within 5–10% of the stagnation-point value at most, as intended with the iso-q model. Because the recession is moderately small, the shape change effects on the surface heat flux and pressure distributions appear to be negligible. As expected, the pressure is much less affected by the shape change where it drops along the surface as the flow at the boundary layer edge accelerates away from the stagnation point toward the corner region. However, an uncoupled TITAN simulation for the nominal iso-q shape is not possible, even though the heat flux variation over the front face of the model appears not to change significantly with time. A peak in the heat flux at the corner region of the model is predicted by CFD simulations for the nominal shape. In a TITAN simulation, this peak causes uneven recession near the corner, yielding an unrealistic indentation, and the TITAN calculation cannot continue with the original heating profile. Usually, uncoupled TITAN simulations of the iso-q models are performed using monotonically decreasing heating and pressure distributions (a modified iso-q shape, with slightly rounded corner) [13,14]. This test was also analyzed by Milos and Chen [14], using a decoupled approach; to avoid the problem with the corner region in their TITAN analysis, they used the modified iso-q geometry. For the present coupled simulations, the problem is solved gradually as the heating distribution is updated in TITAN.

B. Case 2: 12.7-cm Diameter Flat-Faced Model

The 12.70-cm diameter flat-faced cylinder model tests were conducted by the Orion project. These tests (IHF 198 tests) were run to evaluate performance of PICA at nominal heating conditions of 440 W/cm^2 and 32.7 kPa (stagnation-point cold wall heat flux and

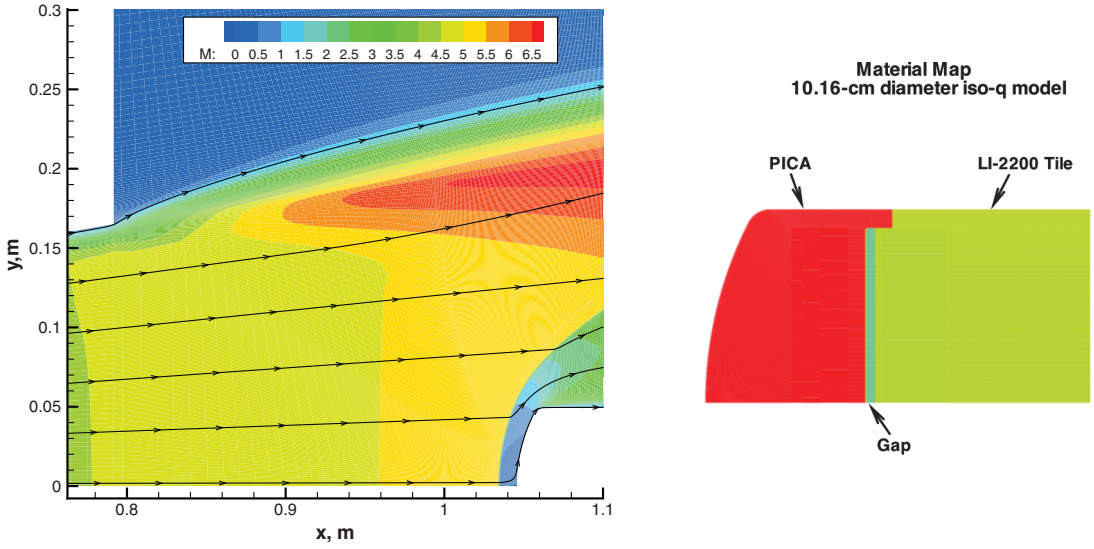

a) Mach number b) Model configuration

Fig. 4 Computed Mach number contours of the iso-q model flowfield and the model interior material map. IHF 13-inch nozzle flow: $p_o = 466$ kPa, $h_o = 21.4$ MJ/kg, and 6.8% Ar in air.

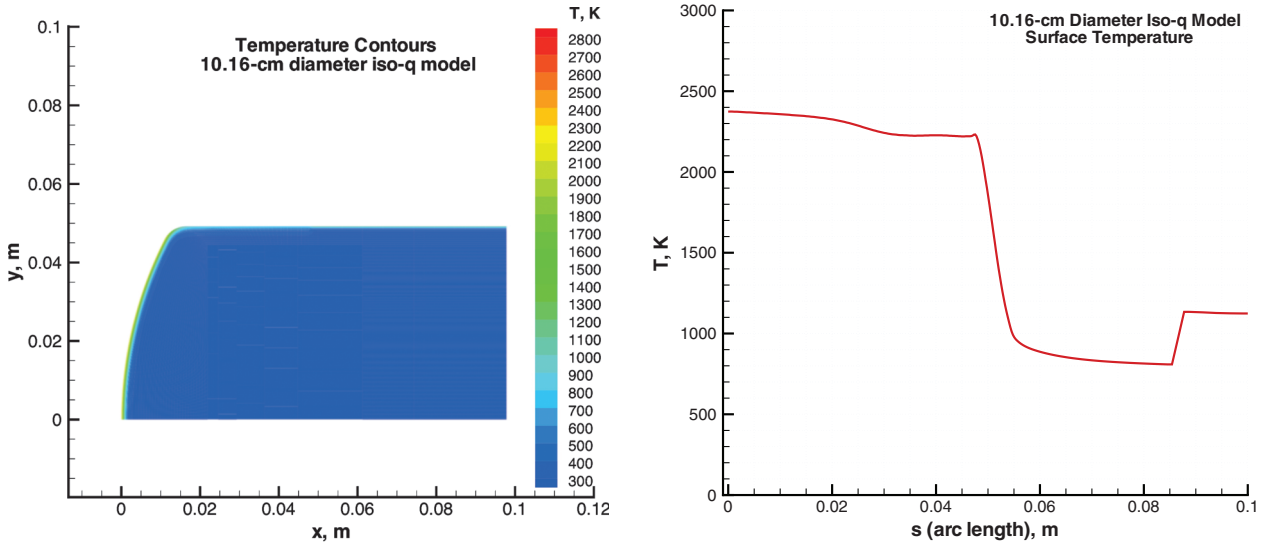

a) t = 0.3 s

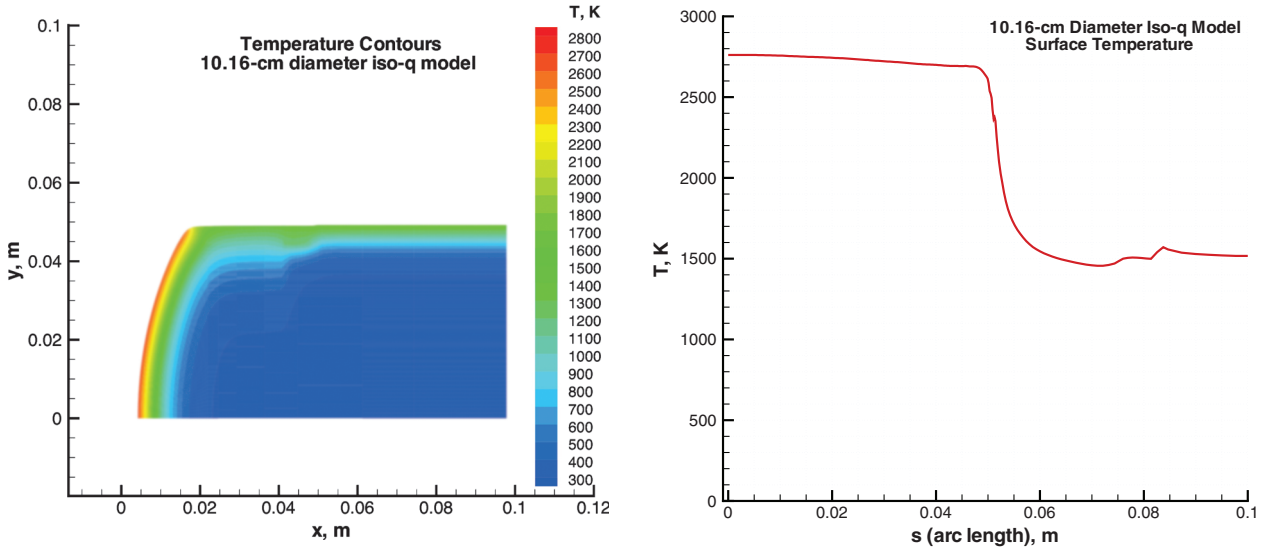

b) t = 34 s

Fig. 5 Computed temperature contours of the iso-q model at two different test times and their surface profiles. IHF 13-inch nozzle flow: $p_o = 466$ kPa, $h_o = 21.4$ MJ/kg, and 6.8% Ar in air.

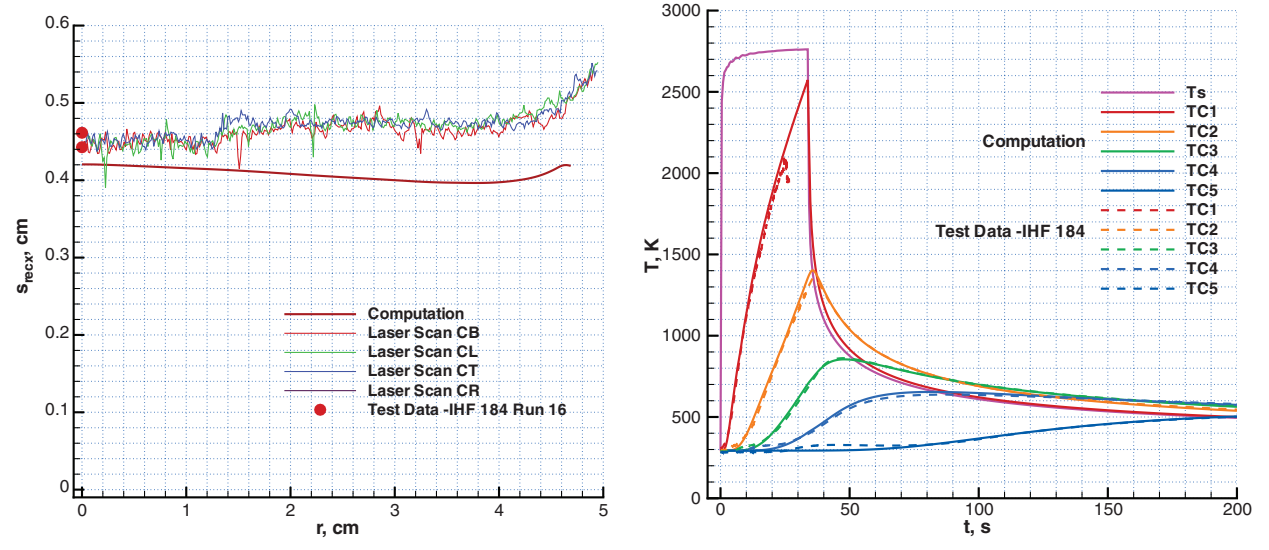

a) Axial recession at t= 34 s

b) In-depth temperatures

Fig. 6 Comparisons of computed recession profiles and thermocouple response with the measurements for the iso-q model. IHF 13-inch nozzle flow: $p_o = 466$ kPa, $h_o = 21.4$ MJ/kg, and 6.8% Ar in air.

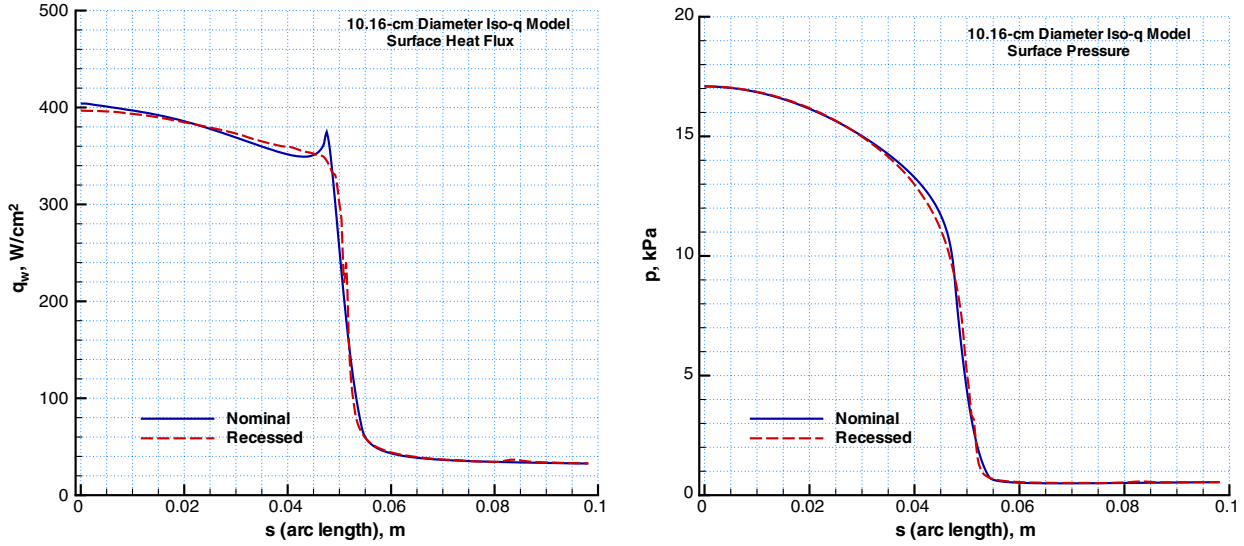

a) Heat flux b) Pressure

Fig. 7 Comparison of computed surface heat flux and pressure distributions of the iso-q model at $t = 0$ s and $t = 34$ s. IHF 13-inch nozzle flow: $p_o = 466$ kPa, $h_o = 21.4$ MJ/kg, and 6.8% Ar in air.

pressure). Similar to case 1, the centerline total enthalpy of the arc-jet test flow is estimated to be 27.3 MJ/kg through CFD simulations, based on the facility and stagnation-calorimeter measurements.

Figure 8 shows the computed Mach number contours of the IHF 13-inch nozzle flow downstream of the nozzle exit. The expansion waves emanating from the corner of the nozzle exit to the test box are clearly observed in the computed Mach number contours. These expansion waves affect the flowfield around the test article, especially for relatively large models (12.70 cm model diameter versus 33.02 cm nozzle exit diameter). For this model, the expansion wave effects are primarily limited to the shoulder region of the model flowfield. Also, in Fig. 8, the material map used for thermal response model simulations is shown. For material response simulations, only the PICA portion of the test model is considered, and the backface of the model is assumed to be insulated. The models were not instrumented with in-depth thermocouples. Therefore, only predictions of the surface recession and the shape change are of interest.

Figure 9 presents the computed temperature contours and surface temperatures of the flat-faced model at two different test times, $t = 0.2$ and $t = 40$ s. At $t = 0.2$ s, the model is still relatively cold. The time $t = 40$ s represents the end of the test, after which the ablated model starts to cool down. At $t = 40$ s, it is clear that the model shape has changed substantially. The shape change causes the surface temperature distribution of the model to become increasingly uniform with time. The corner region of the model started as rounded ($r_c = 0.953$ cm), and the computations show that as the shape changes due to recession, the corner actually becomes sharpened, which was also observed in the tests.

Figure 10 shows the computed surface heat flux and pressure distributions for the nominal and recessed models. Because of the shape change, the heat flux at the stagnation point is increased while the heat flux near the corner region is reduced. As expected, as the test time and recession increase, effects of shape change on the stagnation-point heat flux and its distribution become more important. Again, the pressure distribution is also affected by the shape change but to a smaller extent.

For IHF 198 tests, the recession profiles were measured manually and by use of laser scans of the pre- and posttest models. Figure 11

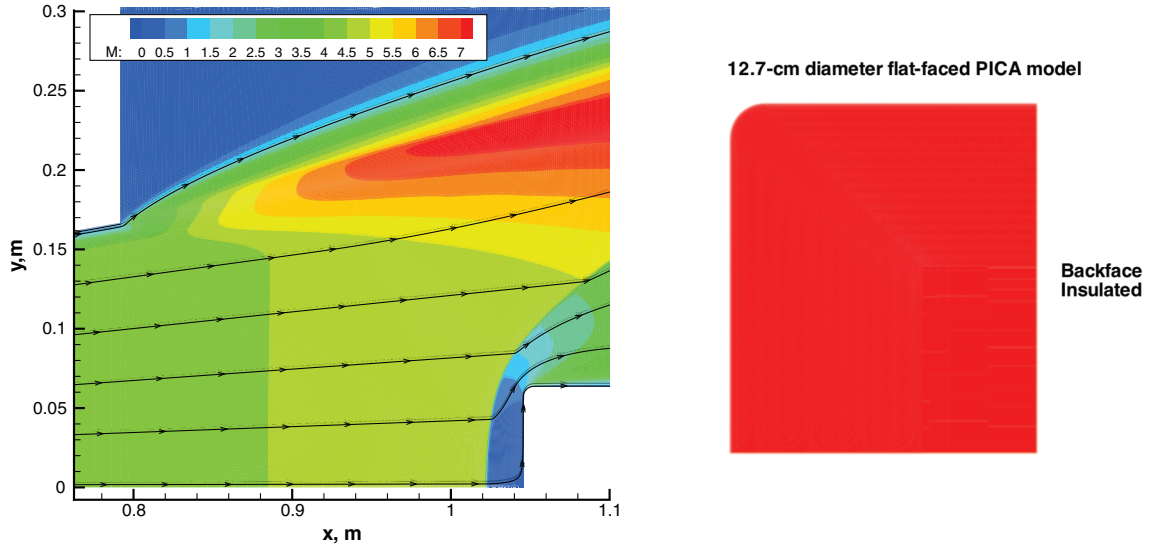

a) Mach number b) Mach number

Fig. 8 Computed Mach number contours of the flat-faced model flowfield and the model interior material map. IHF 13-inch nozzle flow: $p_o = 824$ kPa, $h_o = 27.3$ MJ/kg, and 6.5% Ar in air.

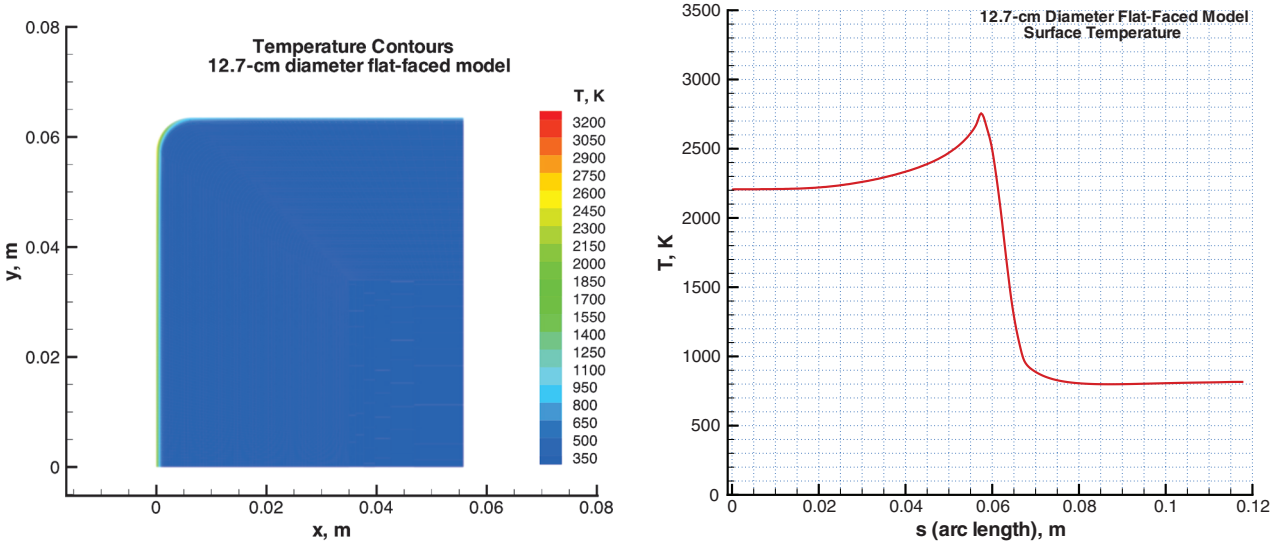

a) t = 0.2 s

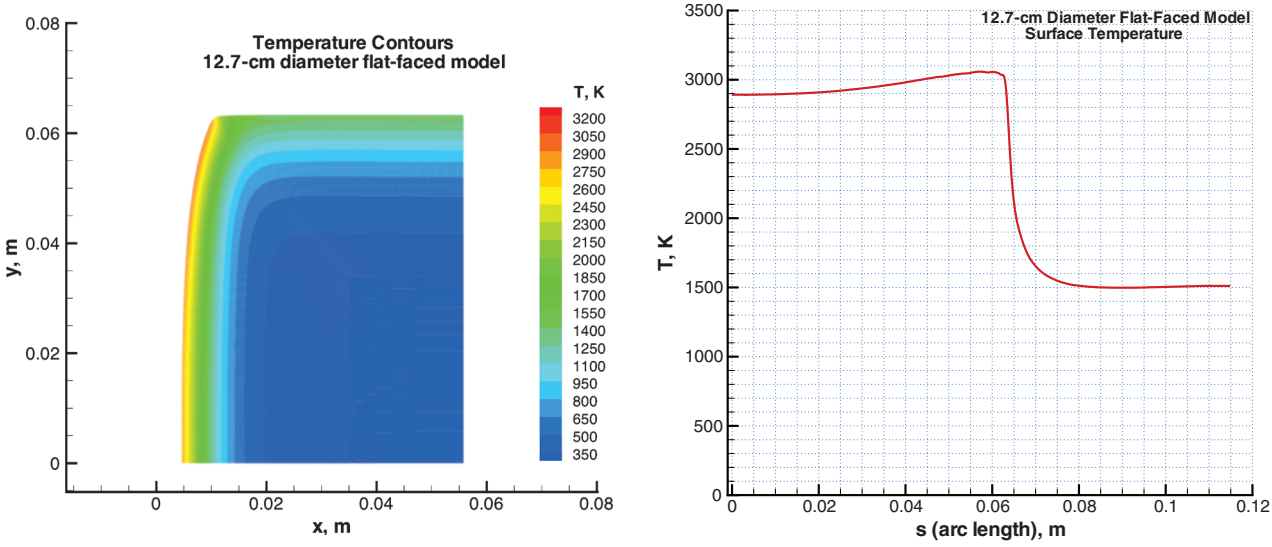

b) t = 40 s

Fig. 9 Computed temperature contours of the flat-faced model at two different test times and their surface profiles. IHF 13-inch nozzle flow: $p_o = 824$ kPa, $h_o = 27.3$ MJ/kg, and 6.5% Ar in air.

shows the measured and computed recession profiles at 40 s. The measurements were obtained for the four quadrants of the model: center to top, bottom, left and right (denoted as CT, CB, CL, CR). The measured stagnation-point recession at $t = 40$ s was 0.543 cm. The computed stagnation-point recession at $t = 40$ s is 0.463 cm, underpredicting the measurements by approximately 15%. When the computations are run longer, the computed recession reaches the measured stagnation-point level at $t = 46.6$ s. The computations appear to overpredict the recession near the corner region where the measurements show relatively flat recession. It has been suggested in the past that the flat-faced models show relatively uniform recession despite the peaked heat flux distribution near the corner region predicted by CFD simulations, possibly because the arc-jet stream has a peaked enthalpy profile.

It is not possible at this time to do a complete sensitivity analysis of computed results for all of the simulation input parameters (reaction rates, relaxation parameters, transport properties, nozzle entrance profiles, etc.). However, sensitivities of the computed heat flux to two arc-jet environment parameters have been investigated: centerline total enthalpy and flow uniformity of the arc-jet flow. The centerline total enthalpy is not a measured parameter; it is deduced from the calorimeter measurements. Because the calorimeter heat flux measurements have an uncertainty of ±10–15%, the estimated total enthalpy has an uncertainty of at least ±10–15%. Although the results are not presented here, computations were also run for ±10% of the nominal total enthalpy of 27.3 MJ/kg, i.e., at 30.03 and 24.57 MJ/kg, keeping the heat flux levels at 27.3 MJ/kg. As expected, at the lower enthalpy, a higher heat transfer coefficient is computed, and as a result a higher recession is predicted. At the higher enthalpy, the reverse is true. The $t = 40$ s predicted stagnation-point recession at the enthalpies of 30.03 and 24.57 MJ/kg are 0.419 and 0.512 cm, respectively.

Even though the distribution of total enthalpy at the nozzle exit was not known for these tests (there were no heat flux calorimeter/pitot surveys available), simulations were performed with varying degrees of nonuniformity, which are differentiated by the ratio of the centerline total enthalpy to the bulk enthalpy, to gage its sensitivity. Figure 12 shows the computed total enthalpy contours for the $h_{ocl}/\bar{h}_o = 1.5$ case, and comparisons of computed surface heat flux distributions using uniform and nonuniform mass flux and total enthalpy profiles at the throat. For these cases, the distributions are varied by keeping the mass flux and total enthalpy constant at the nozzle throat centerline while changing the corresponding bulk quantities. Parabolic profiles at the throat are introduced in the

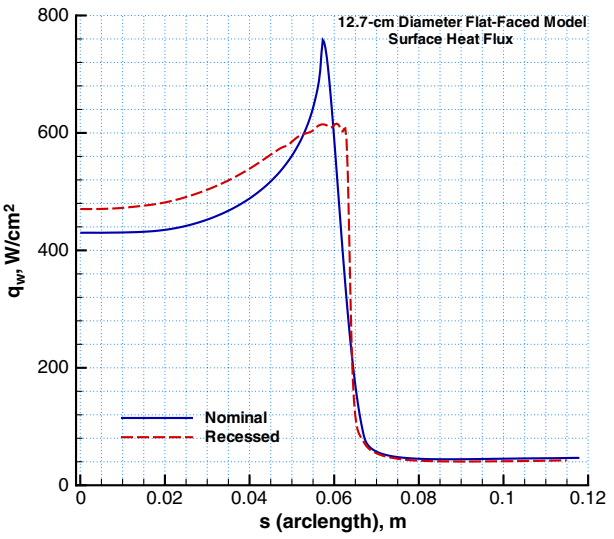

a) Heat flux

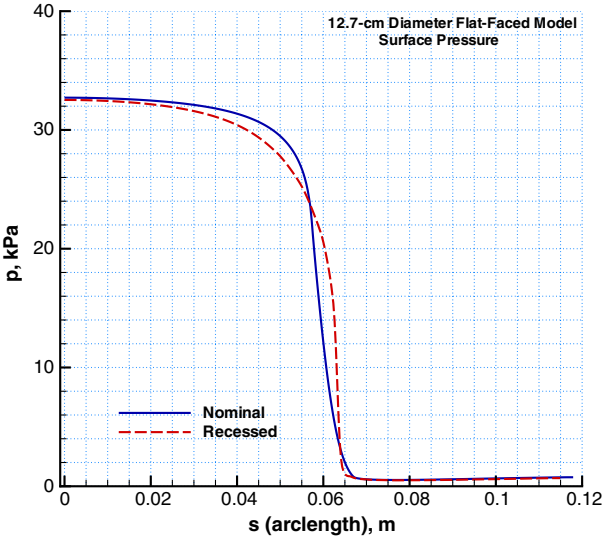

b) Pressure

Fig. 10 Comparison of computed surface heat flux and pressure distributions of the flat-faced model at $t = 0$ s and $t = 40$ s. IHF 13-inch nozzle flow: $p_o = 824$ kPa, $h_o = 27.3$ MJ/kg, and 6.5% Ar in air.

computations in such a way that the centerline estimates of mass flux and total enthalpy are made consistent with the facility total bulk enthalpy estimates and mass flow rate measurements.

The computations indicate that nonuniform total enthalpy and mass flux profiles at the nozzle throat do not affect surface heat flux and its distribution over the model significantly; the centerline total enthalpy is the most important parameter for predicting the heat flux distribution over the model. This is because the streamlines affecting the model flowfield are confined to a narrow region near the centerline, as seen in Fig. 12a. This means that the total enthalpy at the edge of the boundary layer formed over the model surface is effectively close to the centerline total enthalpy. However, were the model size to get larger with respect to the nozzle exit diameter, the nonuniform enthalpy profile would be expected to affect the model flowfield and its heat flux distribution.

C. Case 3: 10.16-cm Diameter Flat-Faced Model

The 10.16-cm diameter flat-faced cylinder model tests were conducted and reported by Covington et al. [12]. These tests (IHF 121 Phase II) were run to evaluate the performance of the Stardust spacecraft heatshield PICA and to address uncertainties in its flight qualification. Although during the IHF 121 test series 2.54, 5.08, and 10.16-cm diameter flat-faced models were tested, only the 10.16-cm diameter model tests are considered here because they were relatively long duration tests, and the models recessed significantly. During the tests, optical pyrometers were used to measure the model surface temperature, and type-R and type-K thermocouples were used to measure in-depth temperatures. For details of the test data and model instrumentation, the reader is referred to [12].

Nominal stagnation-point heat flux and pressure for this case were 580 W/cm^2 and 45.6 kPa. Again, similar to case 1 and case 2, CFD simulations were performed to estimate the centerline total enthalpy based on the facility and stagnation-point calorimeter measurements, and the total enthalpy is estimated to be 26.9 MJ/kg. Covington et al. [12] estimated the total enthalpy to be 29.5 MJ/kg. All of the arc-jet facility/test data were not available to the authors. Perhaps, the 29.5 MJ/kg estimate was based on a Fay–Riddell type correlation instead of CFD simulations. In any case, simulations are performed at 26.9 MJ/kg because the reported stagnation-point heat flux and pressure are reproduced using this enthalpy. Figure 13 shows the

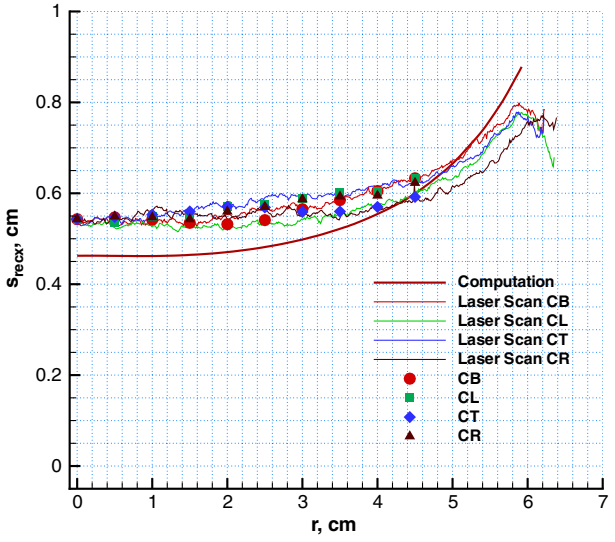

a) Axial recession at $t = 40$ s

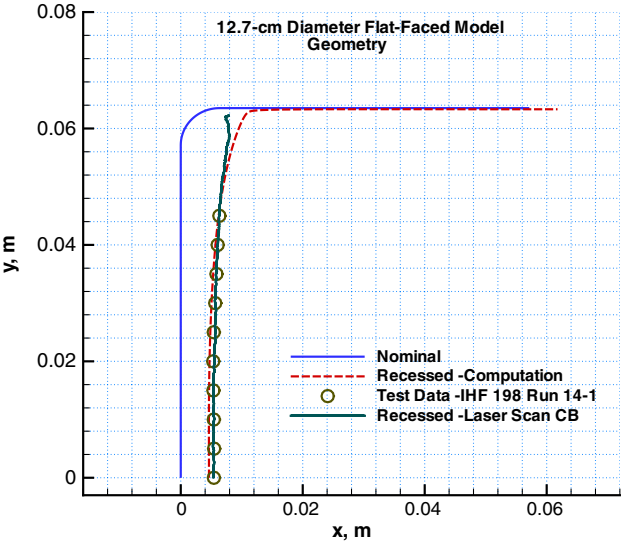

b) Model shape at $t = 40$ s

Fig. 11 Comparisons of computed recession profiles and shape change with the measurements for the flat-faced model. IHF 13-inch nozzle flow: $p_o = 824$ kPa, $h_o = 27.3$ MJ/kg, and 6.5% Ar in air.

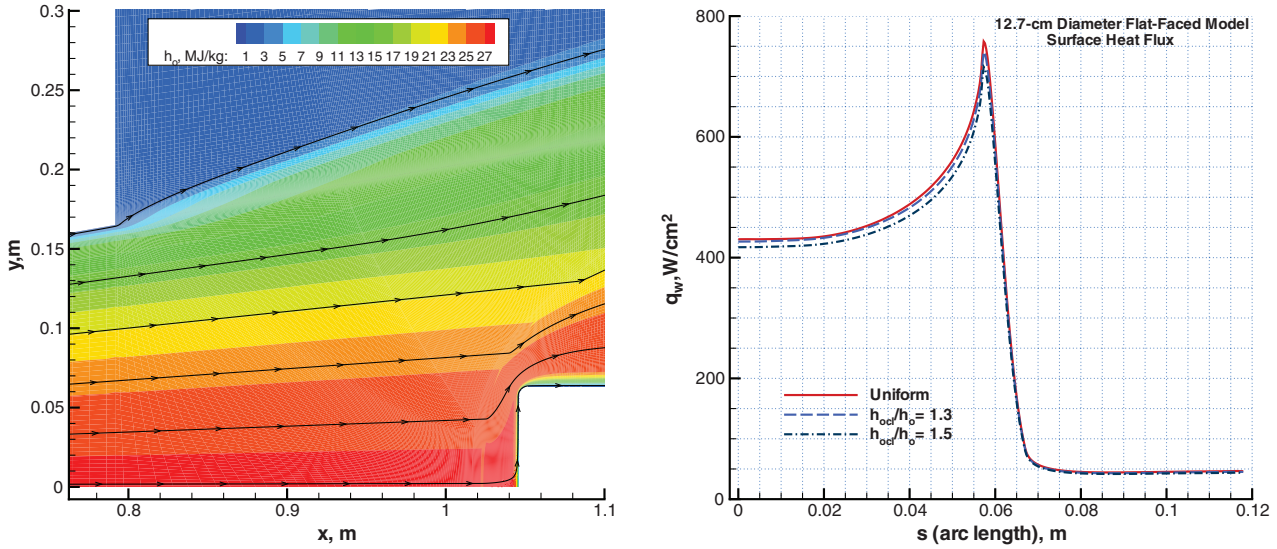

a) Total enthalpy contours, $h_{ocl}/\bar{h}_o = 1.5$ b) Heat flux

Fig. 12 Effect of nonuniform enthalpy profiles on the heat flux distribution of the flat-faced model. IHF 13-inch nozzle flow: $p_o = 824$ kPa, $h_{ocl} = 27.3$ MJ/kg, and 6.5% Ar in air.

computed Mach number contours and the interior material map used for thermal response model simulations. Note that the backface of the AETB-12 tile is assumed to be insulated.

Figure 14 presents the computed temperature contours and surface temperatures of the model at test times, $t = 0.3$, 69, and 86 s. The computations show that significant amounts of recession and shape change occur during the $t = 69$ and $t = 86$ s tests. As in case 2, the shape change occurred in such a way that the surface temperature distribution of the model becomes increasingly uniform with time. The initial temperature discontinuity on the aft flank of the model at $t = 0.3$ s is due to the differences in emissivity and thermal conductivity of the two materials, PICA and AETB-12 (alumina enhanced thermal barrier) tile. At both $t = 69$ and $t = 86$ s, there is a noticeable sidewall recession predicted by the computations. It is also worth mentioning that the radius of curvature for the model surface near the corner region decreases as the model recesses. In other words, the corner sharpens during the arc-jet tests. Sidewall recession and the sharpening of the corner region are also evident from posttest examination of the model.

The posttest photo of Covington et al. [12] (Model 2: Run 15 W, 86 s test, rotated 90°) and computed density contours of the model at 1000 s are presented in Fig. 15. The material density is normalized by the virgin PICA density. The contours provide a qualitative map of where the char layer and pyrolysis zone of the model are. It should be noted that after the heating pulse of the test ends, at $t = 86$ s, pyrolysis and charring processes of the PICA continue during a portion of the cool-down phase. The cool-down calculations up to both 600 and 1000 s were performed, and no noticeable differences can be observed in the density contours between the 600 and 1000 s results. Although it is difficult to make quantitative comparison between the computed density contours and posttest photo, there are definitely qualitative similarities between them. The darkened region near the surface in the photo is indicative of how far the char layer extended from the surface. In the normalized density contours, the region that has values of 0.90 or less may be considered as the char layer. The computed results show that there was no virgin material left after the cool-down, because the normalized density is less than unity everywhere. As mentioned earlier, the material properties of the

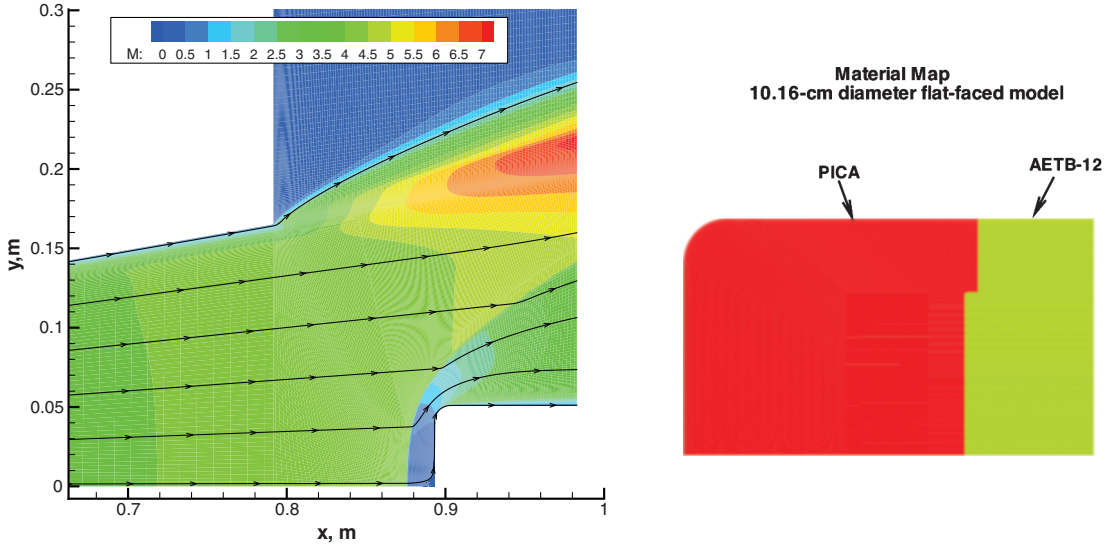

a) Mach number b) Mach number

Fig. 13 Computed Mach number contours of the flat-faced model flowfield and the model interior material map. IHF 13-inch nozzle flow: $p_o = 906$ kPa, $h_o = 26.9$ MJ/kg, and 6% Ar in air.

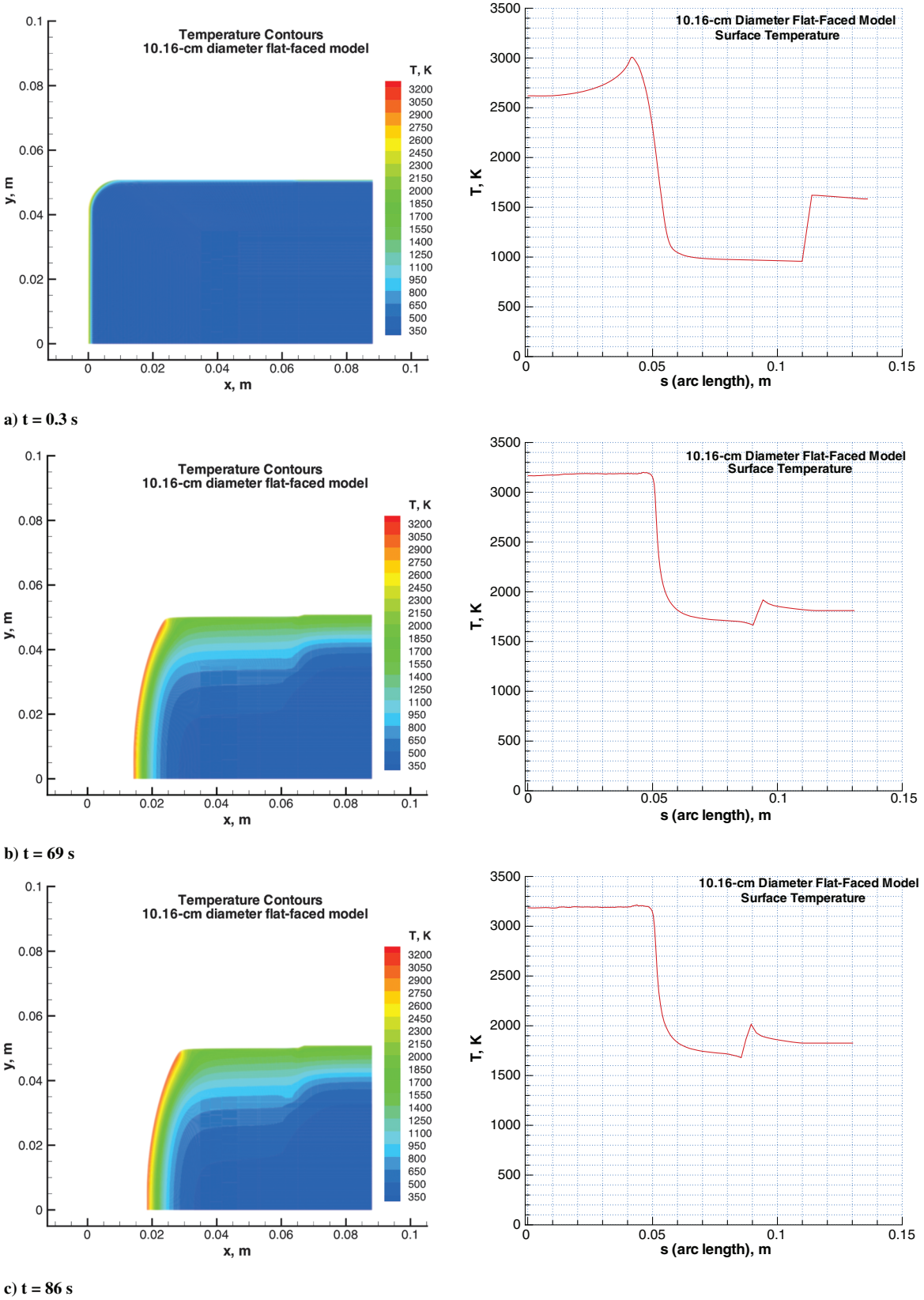

Fig. 14 Computed temperature contours of the flat-faced model at three different test times and their surface profiles. IHF 13-inch nozzle flow: $p_o = 906$ kPa, $h_o = 26.9$ MJ/kg, and 6% Ar in air.

PICA used by Covington et al. [12] are somewhat different from the PICA used by the Orion TPS project. The virgin PICA and char densities reported by Covington et al. were 266 and 210 kg/m^3, respectively. In the present simulations, the computed char density near the surface is aproximately 229 kg/m^3, and the virgin PICA density is 274 kg/m^3.

In Fig. 16, computed stagnation-point recession and heat flux are plotted as functions of time for the flat-faced model. For the 86-s test, simulations were completed in 470 steps (*Gridgen*, DPLR and TITAN runs). Figure 16a also shows the measured stagnation-point recession data. The computations overpredict recession by approximately 17% at 69 s and 26% at 86 s, and the computed

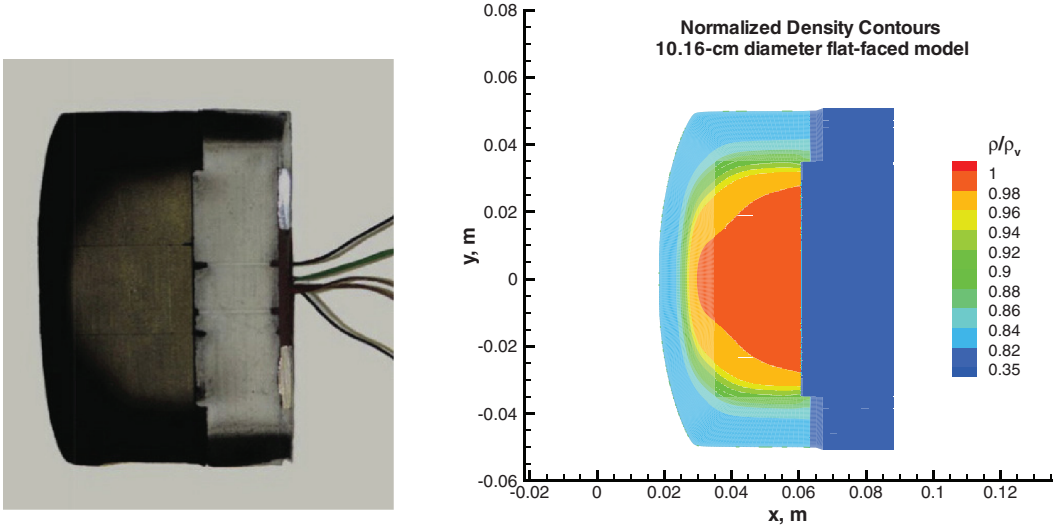

a) Posttest photo, Covington et al. [12] b) Normalized density at $t = 1000$ s

Fig. 15 Posttest photo and computed normalized density contours of the flat-faced model for the 86-s test. IHF 13-inch nozzle flow: $p_o = 906$ kPa, $h_o = 26.9$ MJ/kg, and 6% Ar in air.

stagnation-point recession rate (slope of the recession curve) increases with time. This increase is obviously due to the increase in the heat flux at the stagnation point during the test. Note that the reported recession rate for the 86-s test by Covington et al. [12] is lower than the average recession rate for all of their 10.16-cm data. Figure 16b shows that the computed stagnation-point heat flux increases approximately 30% during the 86-s test as a result of the model shape change. Computations were also performed at 110% of the nominal total enthalpy 26.9 MJ/kg, i.e., at 29.59 MJ/kg, by keeping the heat fluxes at the 26.9 MJ/kg level. As expected, the higher enthalpy translates into a lower heat transfer coefficient, and hence lower recession is predicted. The stagnation-point recession is still overpredicted, although the differences are smaller (6% at 69 s and 14% at 86 s). The centerline total enthalpy estimated by Covington et al. was 29.5 MJ/kg. Also, in Fig. 16, the computed recession at the stagnation point is smoothly increasing in time but the computed heat flux has a semiregular wave pattern. While the reasons for this behavior are not fully understood, there are at least two likely contributors. Although the stagnation-point recession is smoothly increasing, the effective nose radius for the model is not monotonically decreasing due to the shape change. Also, the stagnation-point heat flux computed by DPLR is sensitive to the alignment of grid lines with the bow shock formed in front of the model. Whenever a new grid is generated the alignment of the grid points also changes. Nevertheless, these variations are relatively small compared with the mean value of the heat flux.

Figure 17 illustrates the model shape change and its effect on heat flux distributions over the model. Clearly, during the 86-s test, the model shape has changed, and as a result, the stagnation-point value and distribution of the surface heat flux are significantly altered. Flat-faced cylinder models are traditionally used in arc-jet stagnation tests. As these computations show, if there is significant recession and shape change, their effects must be taken into account to characterize the test environment and to analyze the test data, which requires coupling of the fluid-material simulations. It should also be mentioned that these long duration test simulations (e.g., $t = 86$ s) also provide a model shape that would be more suitable for arc-jet stagnation tests (constant heat flux shape for PICA models).

Figure 18 shows comparisons of computed in-depth temperatures with three thermocouple measurements at two test times. The thermocouples (TC1, TC2, TC3) were placed along the centerline of the model at depths of 0.838, 2.238, and 4.232 cm, respectively, from

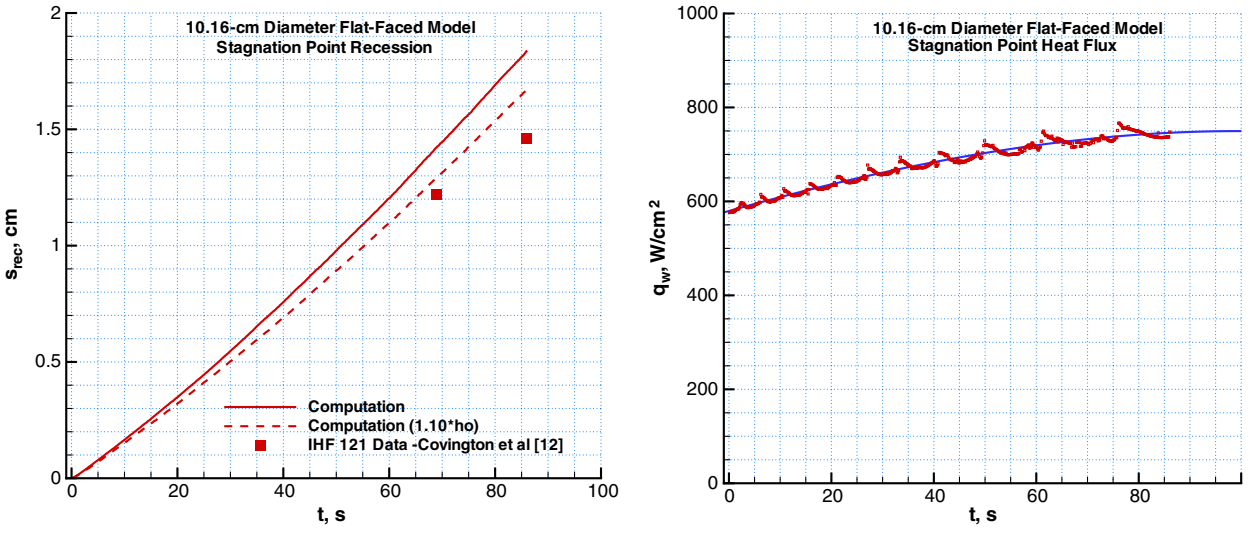

a) Recession vs. time b) Heat flux vs. time

Fig. 16 Computed stagnation-point recession and heat flux as functions of time for the flat-faced model. IHF 13-inch nozzle flow: $p_o = 906$ kPa, $h_o = 26.9$ MJ/kg, and 6% Ar in air.

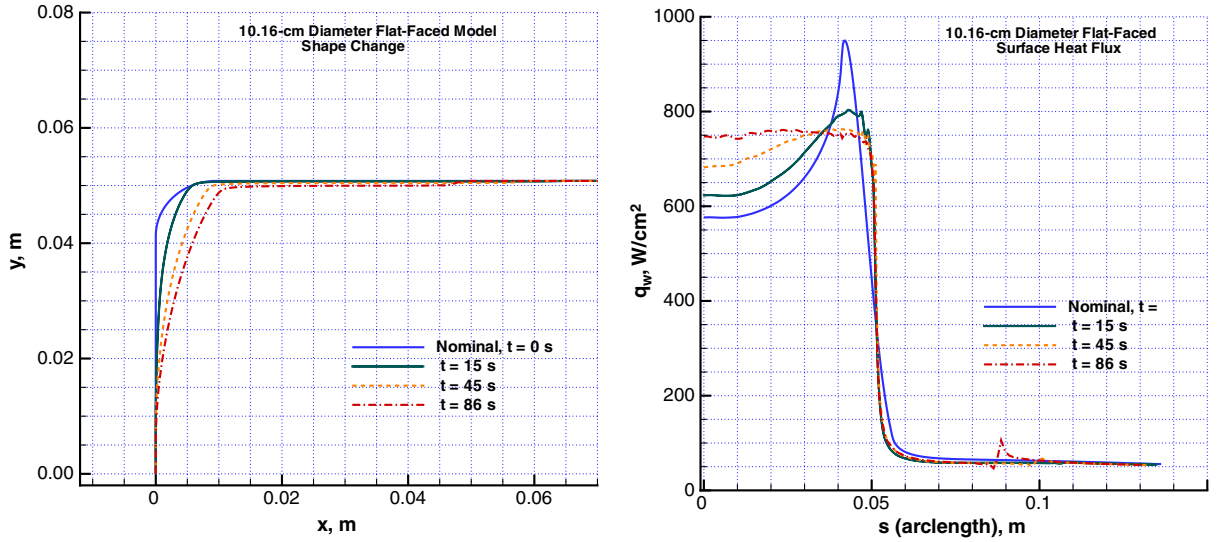

a) Model shape **b) Heat flux**

Fig. 17 Shape change and its effect on heat flux distributions for the flat-faced model. IHF 13-inch nozzle flow: $p_o = 906$ kPa, $h_o = 26.9$ MJ/kg, and 6% Ar in air.

the unablated model surface. Computations reproduce the TC1 measurements reasonably well until thermocouple failure occurs due to high temperatures (approximately up to $t = 35$ s). For TC2 and TC3, the computations only qualitatively agree with the measurements. For the TC2 temperature history, the computations show a faster rise during the heating period and a faster drop during the cooldown phase of the test in comparison with the measurements. Both of these observations are consistent with the fact that the surface recession is overpredicted by the computations. However, for the TC3 location, the computations are significantly lower. Although the material properties of the PICA used in these tests are different from the PICA used in the Orion TPS project arc-jet tests (for which PICAv3.3 model was developed), it is unlikely that these apparent differences in PICA material density and conductivity would be able to explain the discrepancy in the TC3 temperatures.

D. Uncertainties of Computations and Measurements

The axisymmetric CFD computations of the nozzle/test box/model flowfield were performed using multiblock grids with 8.76×10^4 points (the size of the inner computational block over the models being 200×120). For the material response simulations, computational grid sizes were 214×190, 202×220, and 202×220 for case 1, case 2, and case 3, respectively. However, the number of grid points used is only one of the metrics that define a good grid to produce accurate results. Often, grid topology, minimum mesh spacing near the wall, orthogonality of grid lines near the wall, and grid alignment to the shock wave are as important. Based on the authors' judgement, and the limited number of grid refinement studies performed, the authors believe that the grid quality issues of the computations were adequately addressed. However, CFD computations of arc-jet flows, as for hypersonic flight simulations, include uncertainties in many of the model input parameters. It is not possible at this time to do a complete uncertainty analysis of computed results for all of the simulation input parameters. In the authors' opinion, the most important input parameter is the centerline total enthalpy of the arc-jet test flow. The centerline total enthalpy is not a measured parameter; it is directly deduced from the calorimeter heat flux and pitot pressure measurements. A complete uncertainty analysis of the stagnation calorimeter measurements is also not available. However, based on empirical evidence (historical Ames

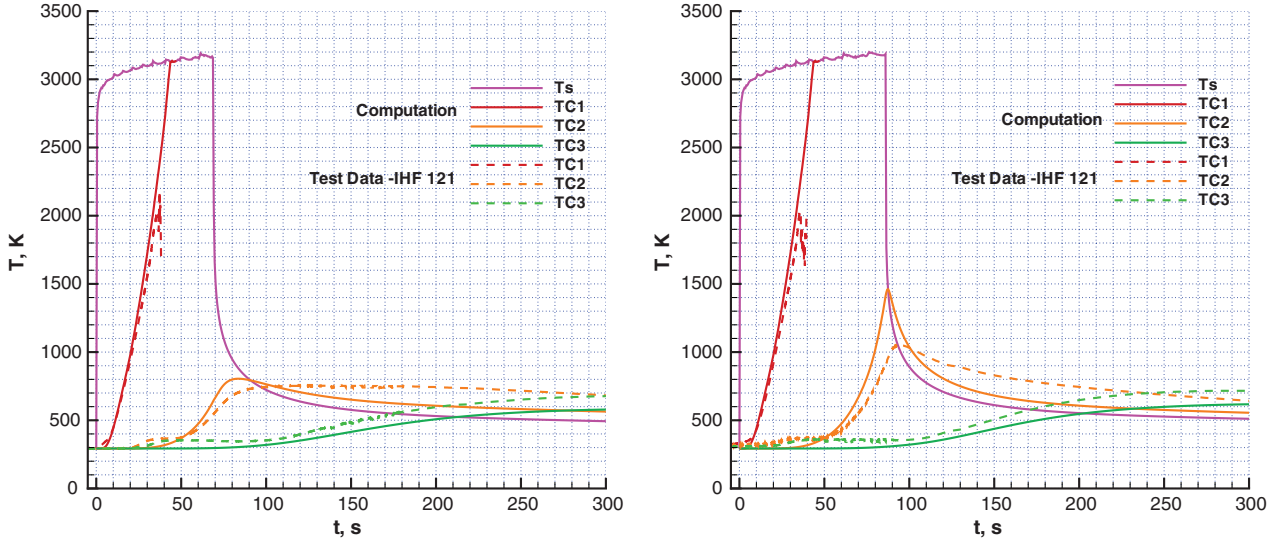

a) Heating pulse until $t = 69$ s **b) Heating pulse until $t = 86$ s**

Fig. 18 Comparisons of computed thermocouple response with the measurements for the flat-faced model. IHF 13-inch nozzle flow: $p_o = 906$ kPa, $h_o = 26.9$ MJ/kg, and 6% Ar in air.

arc-jet data), the calorimeter heat flux measurements are believed to be accurate to within 10–15% and the pitot pressure measurements to within 5%. Therefore, the CFD estimated enthalpy has an uncertainty of at least ±15%, and including other modeling parameters used in CFD, it can be as much as ±20%. Because only fully-catalytic cold wall heat flux predictions are of interest for the material response analysis, effects of model input parameters, such as chemical reaction rates, surface catalysis, diffusion model, etc., on the computed heat flux values are expected to be secondary.

For the Orion TPS project, the recession measurements obtained both manually and by laser scans generally agree to within ±0.5 mm. The in-depth thermocouples generally provide consistent measurements for several arc-jet runs: the thermocouple measured temperatures are estimated to be accurate to within ±1–2%; if the measurement errors related to the thermocouple installations are included, they could be as much as ±5%. The model surface temperatures were measured using one-color and two-color pyrometers. One-color pyrometer measurements in the IHF were found to be more reliable. The measured pyrometer temperatures are believed to be accurate to within ±5%.

V. Conclusions

Coupled fluid-material response analyses of arc-jet stagnation tests conducted in the NASA Ames Research Center 60-MW IHF 13-inch nozzle flow are presented. The fluid analysis includes computational Navier–Stokes simulations of the nonequilibrium flowfield in the facility nozzle and test box as well as the flowfield over the models. The material response analysis includes simulation of two-dimensional surface ablation and internal heat conduction, thermal decomposition, and pyrolysis gas flow. For ablating test articles including shape change, the thermal response/ablation and fluid analyses are coupled to take into account changes in surface heating distribution with shape. The ablating material used in these arc-jet tests was a phenolic impregnated carbon ablator, PICA. The experimental test data included measurements of surface pressure and heat flux for calorimeter models, and measurements of surface recession, surface temperature, and in-depth temperatures for ablating models. Computational predictions of surface recession, shape change, and material thermal response are compared with the experimental measurements for three cases. Computations show that the coupled fluid-material simulations are critical to characterizing the arc-jet test environment properly, and to analyzing the test data obtained using ablating flat-faced models. The iso-q shaped model would be a better choice than a flat-faced model for the stagnation arc-jet tests including significant recession.

The present fluid-material response analysis coupling primarily addresses the effects of the model shape change on heating distribution and recession, which may be sufficient for the analysis and interpretation of the arc-jet test data. However, to understand the physics of PICA ablation and its products, such as injection of the ablation products into the model boundary layer and their interactions with the model flowfield, a higher level of fluid-material coupling should be pursued in the future, in which the surface quantities and ablation products/species from the material response simulations are used as surface boundary conditions in the gas dynamics simulations.

Computational simulations, when validated, can assist test planning, define arc-jet test environments for surface properties of TPS, reduce exploratory testing, and provide a framework for tracing the TPS performance from a ground test facility to flight.

Acknowledgments

The authors would like to thank Al Covington and Imelda Terrazas-Salinas for providing the facility and test data for Interaction Heating Facility 121 tests. This work was funded by the NASA Orion Thermal Protection System Advanced Development and Insight/Oversight Projects. The arc-jet operational capability at NASA Ames Research Center is also supported by NASA-SCAP. The support from the NASA Ames Space Technology Division through contract NNA04BC25C to ELORET Corporation is gratefully acknowledged.

References

[1] Winovich, W., and Carlson, W., "The 60-MW Shuttle Interaction Heating Facility," *25th Instrument Society of America Symposium*, Instrument Society of America, Pittsburgh, PA, May 1979.

[2] Winovich, W., Balakrishnan, A., and Balboni, J., "Experimental and Analytical Derivation of Arc-Heater Scaling Laws for Simulating High-Enthalpy Environments for Aeroassisted Orbital Transfer Vehicle Application," AIAA Paper 85-1006, June 1985.

[3] Peterson, A. B., Nichols, F., Mifsud, B., and Love, W., "Arc Jet Testing in NASA Ames Research Center Thermophysics Facilities," AIAA Paper 92-5041, Dec. 1992.

[4] Terrazas-Salinas, I., and Cornelison, C., "Test Planning Guide for ASF Facilities," Thermophysics Facilities Branch, Space Technology Division, NASA Ames Research Center, March 1999.

[5] Anon., "Thermophysics Facilities Branch Fact Sheet," Thermophysics Facilities Branch, Space Technology Division, NASA Ames Research Center, Jan. 2005.

[6] Stewart, D. A., Squire, T., Gökçen, T., and Henline, W., "Arc-Jet Flight Simulation Tests for X-37 Wing Leading Edge TPS," X-37 Rept. for ARC 05 Task 02, Oct. 2004.

[7] Gökçen, T., and Stewart, D. A., "Computational Analysis of Semi-elliptical Nozzle Arc-jet Experiments: Calibration Plate, Wing Leading Edge," *AIAA Journal*, Vol. 45, No. 1, Jan. 2007, pp. 128–137. doi:10.2514/1.22845; also AIAA Paper 2005-4887, June 2005.

[8] Gökçen, T., Raiche, G. A., Driver, D. M., Balboni, J. A., and McDaniel, R. D., "Applications of CFD Analysis in Arc-Jet Testing of RCC Plug Repairs," AIAA Paper 2006-3291, June 2006.

[9] Gökçen, T., Skokova, K., Balboni, J. A., Terrazas-Salinas, I., and Bose, D., "Computational Analysis of Arc-Jet Wedge Calibration Tests in IHF 6-Inch Conical Nozzle," AIAA Paper 2009-1348, Jan. 2009.

[10] Chen, Y.-K., Milos, F. S., and Gökçen, T., "Loosely Coupled Simulation for Two-Dimensional Ablation and Shape Change," AIAA Paper 2008-3802, June 2008.

[11] Tran, H., Johnson, C. E., Rasky, D. J., Hui, F. C., Hsu, M.-T., Chen, T., Chen, Y.-K., Paragas, D., and Kobayashi, L., "Phenolic Impregnated Carbon Ablators (PICA) as Thermal Protection Systems for Discovery Missions," NASA TM-110440, April 1997.

[12] Covington, M. A., Heinemann, J. M., Goldstein, H. E., Chen, Y.-K., Terrazas-Salinas, I., Balboni, J. A., Olejniczak, J., and Martinez, E. R., "Performance of a Low Density Ablative Heat Shield Material," *Journal of Spacecraft and Rockets*, Vol. 45, No. 2, March–April 2008, pp. 237–247. doi:10.2514/1.12403; also AIAA Paper 2004-2273, June 2004.

[13] Milos, F. S., and Chen, Y.-K., "Two-Dimensional Ablation, Thermal Response and Sizing Program for Pyrolyzing Ablators," *Journal of Spacecraft and Rockets*, Vol. 46, No. 6, November–December 2009, pp. 1089–1099. doi:10.2514/1.36575; also AIAA Paper 2008-1223, Jan. 2008.

[14] Milos, F. S., and Chen, Y.-K., "Ablation and Thermal Response Property Model Validation for Phenolic Impregnated Carbon Ablator," AIAA Paper 2009-262, Jan. 2009.

[15] Wright, M. J., Candler, G. V., and Bose, D., "Data-Parallel Line Relaxation Method for the Navier-Stokes Equations," *AIAA Journal*, Vol. 36, No. 9, Sept. 1998, pp. 1603–1609. doi:10.2514/2.586

[16] Park, C., *Nonequilibrium Hypersonic Aerothermodynamics*, Wiley, New York, 1990, Chap. 4.

[17] Park, C., "Assessment of a Two-Temperature Kinetic Model for Dissociating and Weakly Ionizing Nitrogen," *Journal of Thermophysics and Heat Transfer*, Vol. 2, No. 1, 1988, pp. 8–16. doi:10.2514/3.55

[18] Chen, Y.-K., and Milos, F. S., "Two-Dimensional Implicit Thermal Response and Ablation Program for Charring Materials," *Journal of Spacecraft and Rockets*, Vol. 38, No. 4, July–Aug. 2001, pp. 473–481. doi:10.2514/2.3724

[19] Chen, Y.-K., Milos, F. S., Reda, D. C., and Stewart, D. A., "Graphite Ablation and Thermal Response Simulation Under Arc-Jet Flow Conditions," AIAA Paper 2003-4042, June 2003.

[20] Chen, Y.-K., Gökçen, T., and Edquist, K. T., "Two-Dimensional Ablation and Thermal Response Analyses for Mars Science Laboratory Heatshield," AIAA Paper 2009-4235, June 2009.

[21] "*Gridgen*, Version 15.11," Pointwise, Inc., Fort Worth, TX.